Supporting Information for

Highly Efficient Electric-Field Control of Giant Rashba Spin-Orbit Coupling in Lattice-Matched InSb/CdTe Heterostructures

Yong Zhang[1,2,3,‡], *Fenghua Xue*[1,2,3,‡], *Chenjia Tang*[4,5], *Jiaming Li*[1,2,3], *Liyang Liao*[6], *Lun Li*[1,2,3], *Xiaoyang Liu*[1,2,3], *Yumeng Yang*[1], *Cheng Song*[6], *and Xufeng Kou*[1,4] *

[1] School of Information Science and Technology, ShanghaiTech University, Shanghai 200031, China
[2] Shanghai Institute of Microsystem and Information Technology, Chinese Academy of Sciences 200050, China
[3] University of Chinese Academy of Sciences, Beijing 101408, China
[4] ShanghaiTech Laboratory for Topological Physics, ShanghaiTech University, Shanghai 200031, China
[5] School of Physical Science and Technology, ShanghaiTech University, Shanghai 200031, China
[6] Key Lab Advanced Materials (MOE), School of Materials Science and Engineering, Tsinghua University, Beijing 100084, China
‡ These authors contributed equally to this work.
* Corresponding author Email: kxf2323@gmail.com (X.K.).

1. Magento-resistance data of the InSb/CdTe heterostructures.

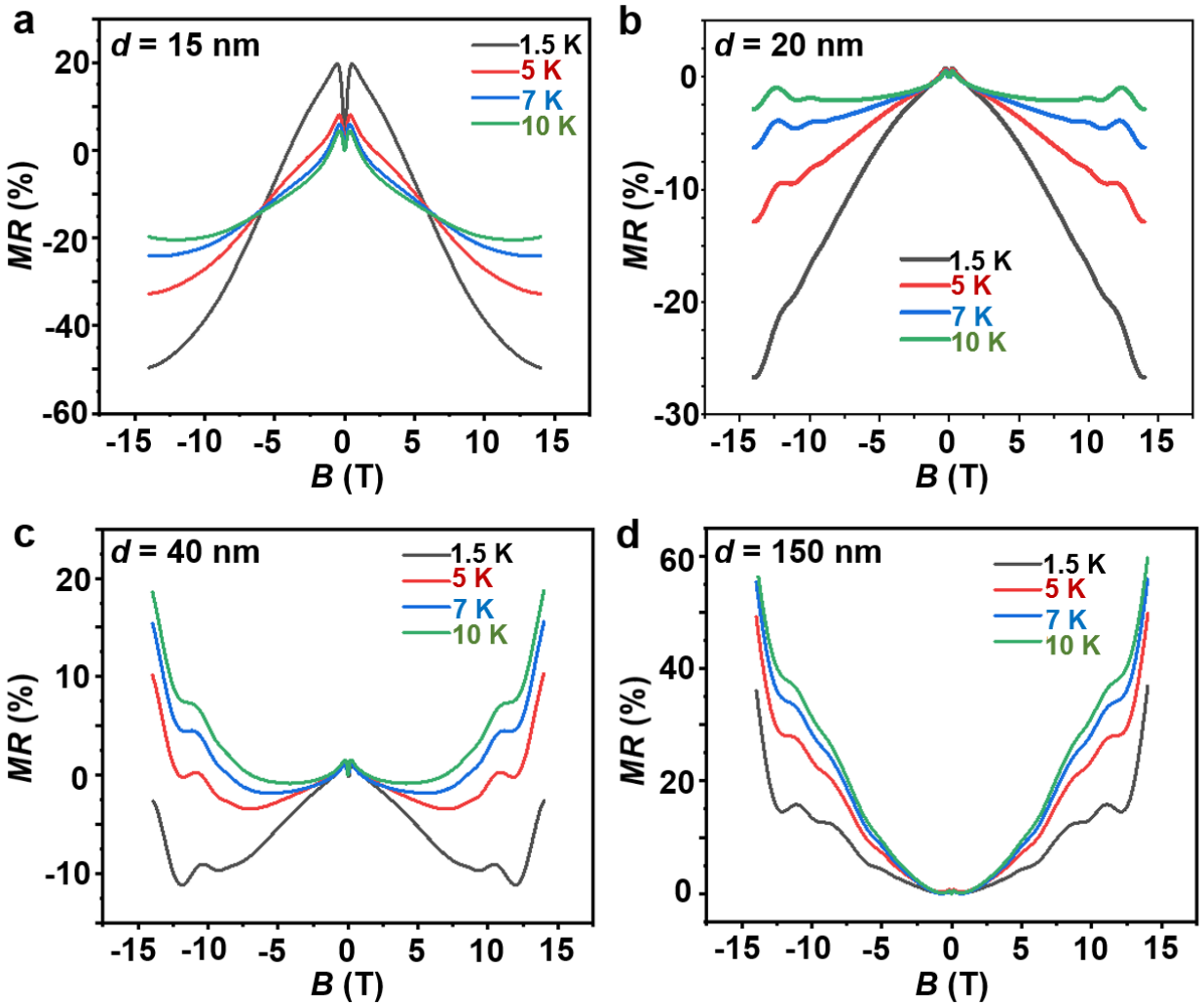

Figure S1. Temperature-dependent magneto-resistance data of the InSb/CdTe heterostructures with different top InSb layer thickness (a) d = 15 nm, (b) 20 nm, (c) 40 nm, and (d) 150 nm. With the increase of d, the overall MR slope changes from negative to positive, and Shubnikov de Haas (SdH) quantum oscillations are observed in the d = 40 and 150 nm InSb/CdTe samples.

According to the classical Hall effect,[1] when electrons are subjected to an external perpendicular magnetic field, the Lorentz force would deflect the electrons away from their original conduction direction. In a bulk semiconductor with a single carrier type (*e.g.,* electron for a *n*-type material), the electron transport is described by $v = \mu(\boldsymbol{E} + v \times \boldsymbol{B})$, where v is the electron velocity, μ is the carrier mobility, $\boldsymbol{E}$ and $\boldsymbol{B}$ are the

external electrical and magnetic fields, respectively.[2] As a result, the magnetoresistance (MR) is proportional to $(1 + \mu B^2)$. However, in our MBE-grown InSb/CdTe heterostructures, we find that the MR curve would deviate from the conventional positive parabolic shape as the top InSb layer thickness is reduced (Figure S1). For the ultra-thin InSb/CdTe(1.2 μm) samples (d = 15 nm and 20 nm), their overall magneto-transport behaviors are dominated by the large negative MR background at cryogenic temperatures (Figures S1a-b). It is noted that negative MR results are also observed in disordered topological insulators[2] and oxide heterostructures (*e.g.*, $LaAlO_3/SrTiO_3$). [3] Besides, it is proposed that the presence of short-range impurity scattering would cause a strong negative MR in the two-dimensional conduction channel.[4] Therefore, we may conclude that the thickness-dependent MR data might imply the unique scattering mechanism associated with the strong spin-orbit coupling in our InSb/CdTe heterostructures.

Additionally, we should point out that in order to quantitatively investigate the weak anti-localization (WAL) behavior under the low magnetic fields, we have re-plotted the magneto-transport data on the basis of conductance by using the reciprocal resistance-to-conductance (ρ - σ) tensor conversion

$$\sigma_{xx} = \frac{\rho_{xx}}{\rho_{xx}^2 + \rho_{xy}^2}, \quad \sigma_{xy} = \frac{\rho_{xy}}{\rho_{xx}^2 + \rho_{xy}^2} \tag{S1}$$

where ρ_{xx}/σ_{xx} and ρ_{xy}/σ_{xy} are the longitudinal and Hall resistance/conductance, respectively. Such data process method has been adopted to construct Figures 1-4 of the main manuscript.

2. Data fitting and parameter extraction from the WAL results.

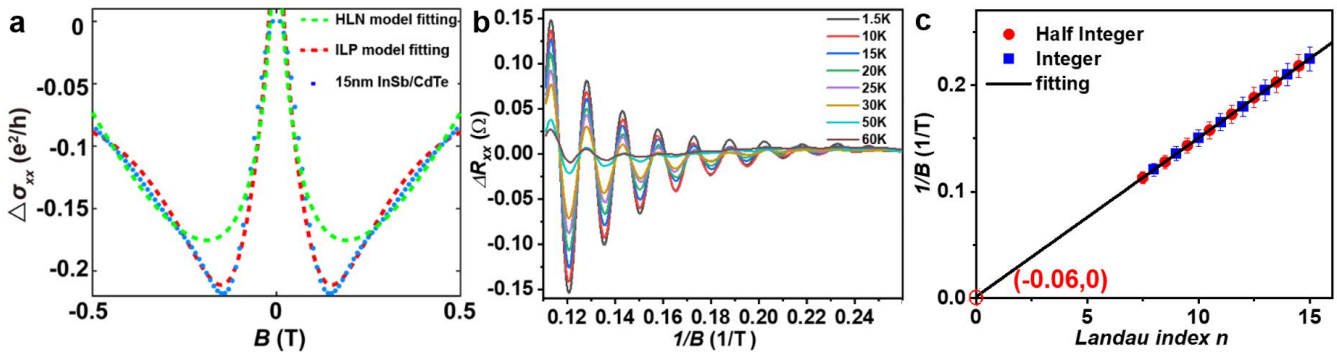

Figure S2. Key parameters extraction from the magneto-transport results. (a) Comparison of the data fitting results between the ILP model and the HLN theory. (b) SdH oscillation patterns as a function of 1/*B* at different temperatures. (c) The Landau index *n versus* 1/*B*. The integer (ΔR_{xx} valleys in Figure S2b) and half-integer indices (ΔR_{xx} peaks) fall into a straight line with the *x*-axis intercept corresponding to a zero Berry phase.

Owning to the strong energy band-bending in our InSb/CdTe heterostructures, it is expected that the resulting giant interfacial Rashba SOC can generate large effective magnetic field $\boldsymbol{B}_{\mathbf{eff}}$ and drive the D'yakonov-Perel (DP)-type spin-precession process during carrier transport.[5] Accordingly, we have managed to apply the Iordanskii, Lyanda-Geller, and Pikus (ILP) model to capture both temperature- and gate-dependent WAL results of the InSb/CdTe samples investigated in the main manuscript.

On the other hand, it is known that the Elliot-Yafet (EY) spin-relaxation mechanism, which considers the spin-flip due to the elastic-scatterings, would also cause the WAL/WL effect in materials with spin degenerated bands [6]. In this regard, the Hikami, Larkin, and Nagaoka (HLN) theory is used to quantify the magnetoconductance correction:[6]

$$\Delta\sigma_{xx}(\boldsymbol{B}) = \sum_{i=0,1} \frac{\alpha_i e^2}{2\pi^2\hbar}\left[\Psi\left(\frac{l_B^2}{l_{\varphi i}^2}+\frac{1}{2}\right)-\ln\left(\frac{l_B^2}{l_{\varphi i}^2}\right)\right] \quad \text{(S2)}$$

where $\boldsymbol{e}$ is the electron charge, $\hbar$ is the reduced Planck constant, Ψ is the digamma function, $l_B = \sqrt{\hbar/4eB}$

is the magnetic length, $l_{\varphi i}$ (i = 1, 2) is the characteristic phase-coherent length, and the coefficients α_1 and α_2 stand for the weights of the WAL and WL contributions, respectively (*i.e.*, α = -1/2 for single channel and α = -1 for two channels).[7] To address this point, we have tried to fit our low-field MC data with Eq. (S2), and Figure S2a shows the fitting result on one dataset of the mm-size InSb(15 nm)/CdTe(1.2 μm) device (T = 10 K). Besides, although few experimental data points can be relatively fitted by the HLN model, yet the extracted weights coefficients are too high ($\alpha_i > 3000$) to be trusted. Along with the linear $\tau_{SO} - {\tau_{tr}}^{-1}$ relation obtained in Figure S4, we may conclude that the large WAL cusps in our InSb/CdTe samples are indeed originated from the DP spin-orbit relaxation mechanism.

Additionally, we have utilized the high-field Shubnikov de Haas (SdH) quantum oscillation data to probe the Fermi surface properties of the InSb/CdTe heterostructures. Benefiting from the high electron mobility and large g-factor of InSb, the sample is driven into the quantum transport regime when B > 4.5 T, and pronounced SdH oscillations can be observed up to 60 K. Figure S2b displays the temperature-dependent normalized oscillating resistance amplitude ΔR_{xx} *versus* 1/B after subtracting their high-field MR backgrounds. All the data exhibit the same single oscillatory frequency of F = 68.72 T from the fast Fourier transform spectra. Moreover, the Landau index plot is provided in the Inset of Figure S2c where the peaks and the valleys of ΔR_{xx} follow a straight line with respect to 1/B, hence revealing the high-mobility nature of the InSb layer with zero Berry phase .

3. Temperature-dependent phase-coherent length of the InSb/CdTe samples.

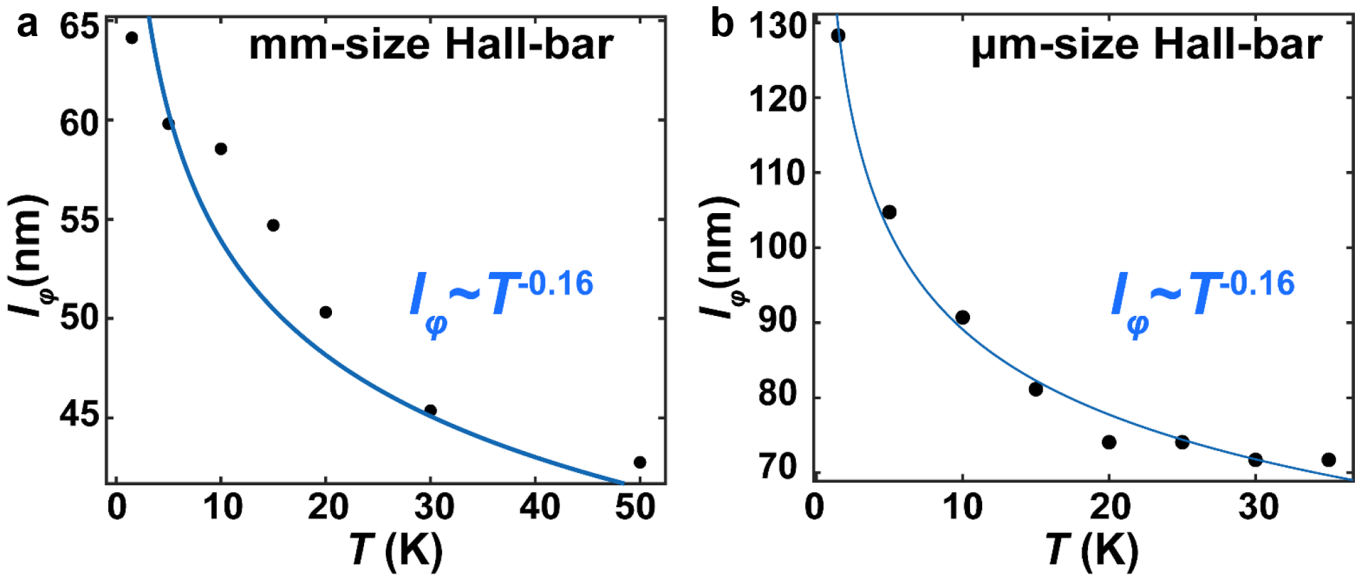

Figure S3. Temperature-dependent phase-coherent length of the InSb(15 nm) /CdTe(1.2 μm) heterostructures in (a) mm-size Hall-bar device (re-captured from Figure 1e) and (b) μm-size field-effect transistor (FET). Both curves follow the same $l_\varphi \propto T^{-\gamma}$ relation with $\gamma = 0.16$.

In the manuscript, we have highlighted the importance of the phase-coherent length (l_φ) on the observation of the WAL effect, and showed that l_φ of different InSb/CdTe samples all decrease monotonically with elevated temperature (Figure 3b). In fact, the phase-coherent length is determined by the inelastic scatterings, and its temperature-dependent response follows a generic $l_\varphi \propto T^{-\gamma}$ correlation, where $\gamma = 0.5$ is for electron-electron scattering and $\gamma = 1$ is for electron-phonon interaction [8]. In our case, it is seen that the phase-coherent length in both the mm-size Hall bar (re-captured from Figure 1e) and the μm-size top-gate FET device exhibit the power-law relation of $l_\varphi \propto T^{-0.16}$ within the $T = 1.5$ K ~ 50 K range, and the reduced γ from the ideal 0.5 value may suggest the presence of additional dephasing mechanisms in our InSb/CdTe heterostructures.[9]

4. Correlation between the spin-orbit relaxation time and the momentum-scattering time.

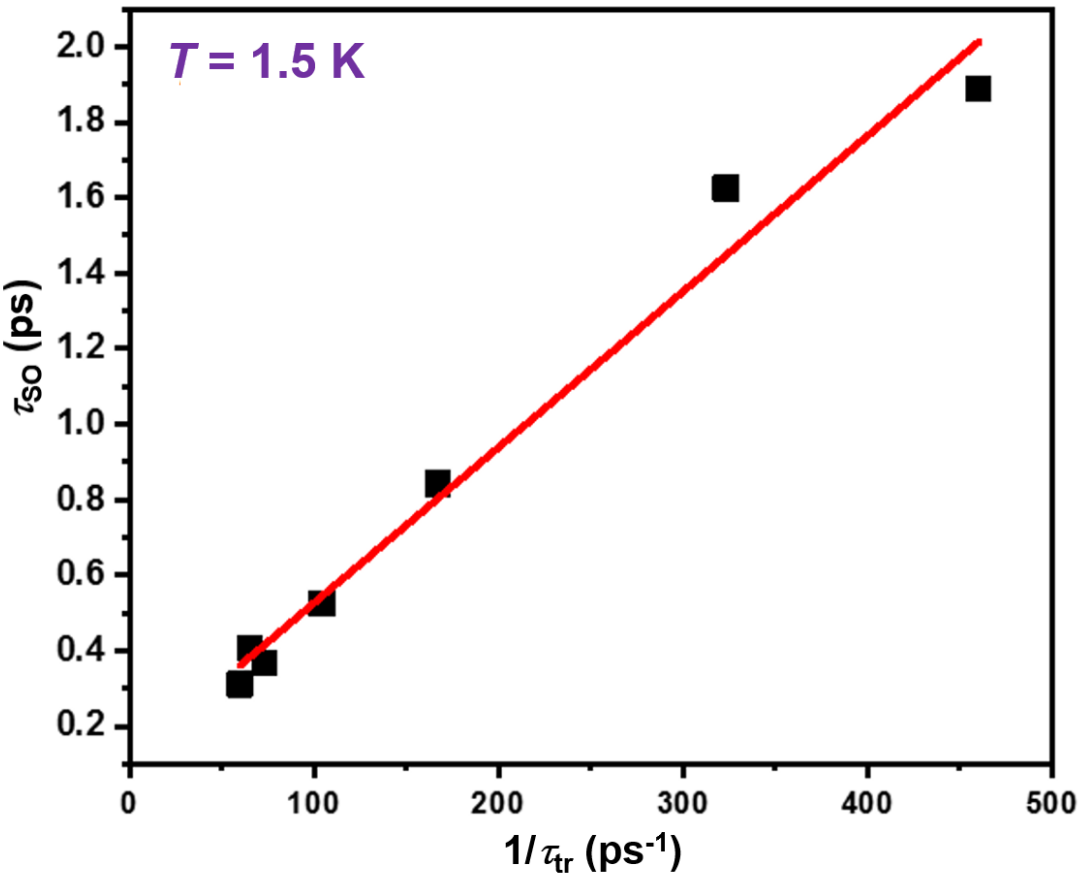

Figure S4. Spin-orbit relaxation time τ_{SO} as a function of the momentum-scattering rate τ_{tr}^{-1} of the InSb(15 nm)/CdTe(1.2 μm) sample. The data are obtained from the gate-dependent magneto-transport measurements in Figure 4.

In the manuscript and Supporting Information S2, we have identified the dominant DP spin-relaxation mechanism in our InSb/CdTe heterostructures. Given that the spin precession is caused by the Rashba SOC-induced effective magnetic field $\boldsymbol{B}_{\mathbf{eff}} = \boldsymbol{p} \times \boldsymbol{E}$ (where $\boldsymbol{E}$ is the electric field), the scattering process that changes the electron momentum $\boldsymbol{p}$ would fluctuate $\boldsymbol{B}_{\mathbf{eff}}$ and in turns affect the spin relaxation.[10] As a result, the spin-orbit relaxation time τ_{SO} is expected to be inversely proportional to the momentum-scattering time τ_{tr}.[11]

Experimentally, we use the gate-dependent magneto-transport data to justify the above scenario in our

InSb(15 nm)/CdTe(1.2 μm) FET device. Specifically, the spin-orbit relaxation time $\tau_{SO} = \hbar/4eDB_{SO}$ (D is the diffusion constant) can be obtained from the fitted B_{SO} in the ILP model, while the momentum-scattering time $\tau_{tr} = \mu m^*/e$ is determined by the electron mobility through ordinary Hall measurement[8]. Figure S3 shows that the extracted $\tau_{SO} - \tau_{tr}^{-1}$ result of the InSb/CdTe sample indeed follows the linear relationship, hence validating the use of the ILP model and relevant arguments in the manuscript.

5. Temperature-dependent longitudinal conductance in the InSb/CdTe heterostructures.

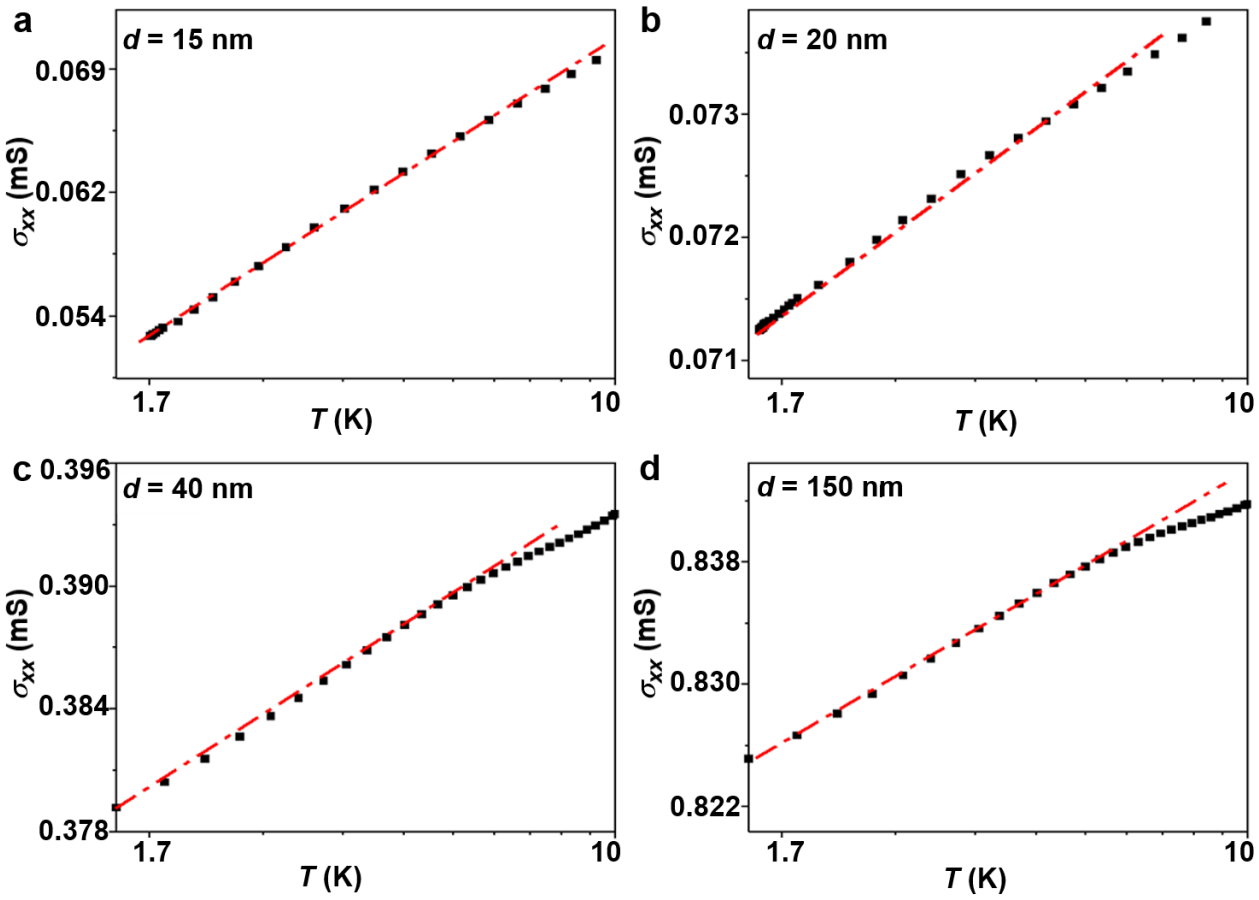

Figure S5. Temperature-dependent longitudinal conductance of the InSb/CdTe heterostructures with different top InSb layer thickness (a) d = 15 nm, (b) 20 nm, (c) 40 nm, and (d) 150 nm, respectively. The linear σ_{xx} - log(T) correlation in all samples confirms the two-dimensional transport feature at deep cryogenic temperatures.

One distinctive feature of the magneto-transport results of the InSb/CdTe heterostructures is that the pronounced WAL effect can be observed in samples with the top InSb layer thickness ranging from 15 nm to 150 nm (Figure 2). To further investigate its underlying physics, we provide the temperature-dependent conductance information of the four samples in Figure S5. It is clearly seen that all the σ_{xx} - log(T) data exhibit the linear relationship at deep cryogenic temperatures (T < 10 K), which confirmed the two-dimensional signature of the quantum interference-induced transport in the InSb/CdTe heterostructures.[12]

6. Temperature-dependent longitudinal conductance in the InSb/CdTe heterostructures.

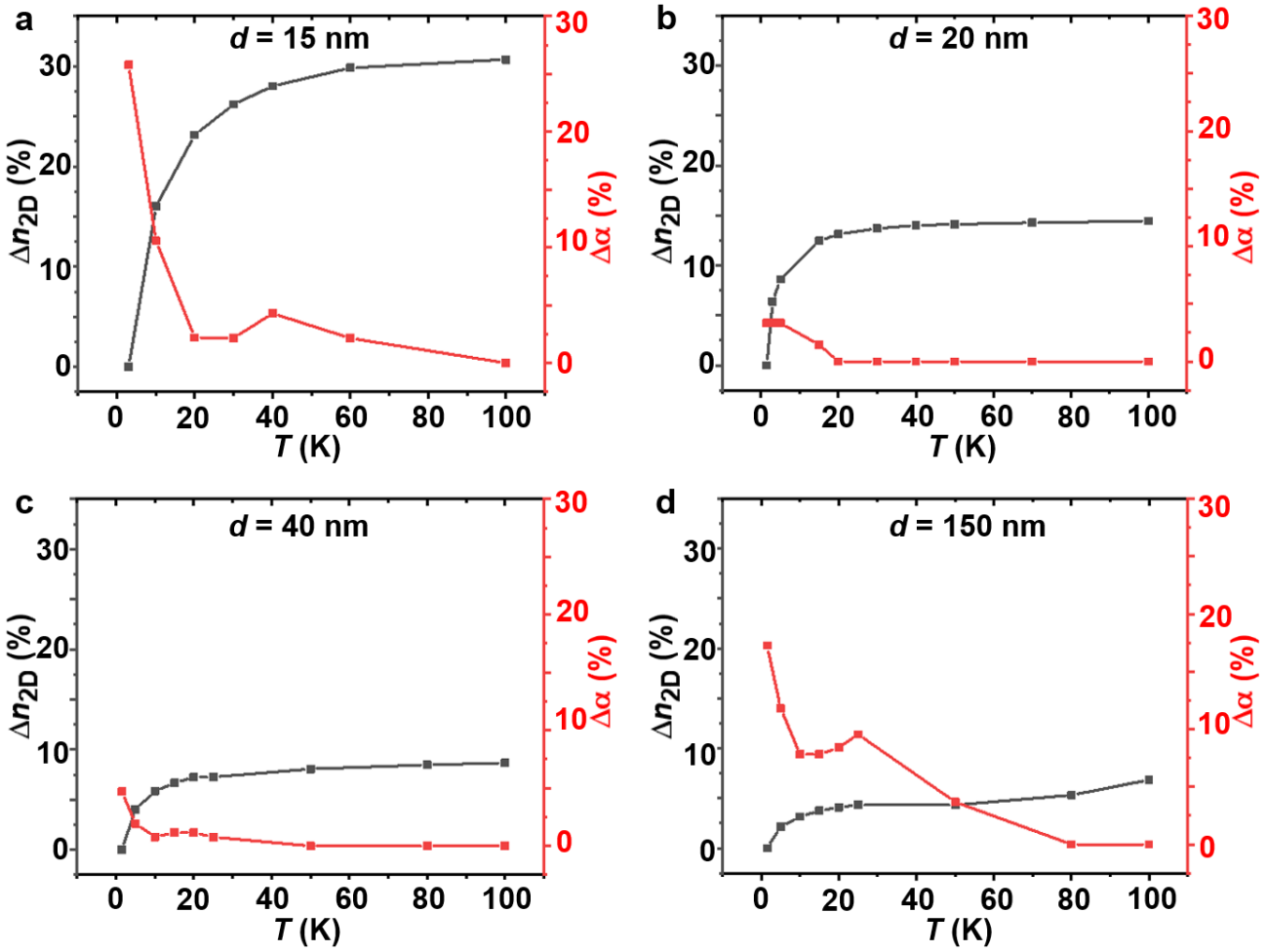

Figure S6. Temperature-dependent normalized carrier density (Δn_{2D}) and Rashba coefficient ($\Delta\alpha_R$) evolutions in the InSb/CdTe heterostructures with different top InSb layer thickness (a) d = 15 nm, (b) 20 nm, (c) 40 nm, and (d) 150 nm. When T < 20 K, the carrier densities become smaller in all samples due to the carrier freeze-out effect, and the suppression of n_{2D} leads to the increase of the Rashba coefficient α_R accordingly.

As illustrated in Figure 3a, the Rashba coefficient of the InSb(15 nm)/CdTe(1.2 μm) sample experiences a sharp increase when the base temperature is cooled down below 10 K, and we have attributed it to the suppression of the itinerant electrons at deep cryogenic temperatures. In fact, given the same nature of the carrier freeze-out effect in semiconductors, the lowering of the carrier density n_{2D} is also observed in other

samples (d = 20, 40, and 150 nm) investigated in the manuscript, as shown in Figure S6. As a result, the corresponding α_R of these three samples are found to increase (although by a much smaller percentage as compared with the d = 15 nm counterpart) when T < 10 K. Accordingly, it is suggested that the reduction of bulk conduction would enhance the interfacial Rashba SOC in our InSb/CdTe heterostructures, and such findings are consistent with the gate-dependent α_R data in Figure 4.

7. Temperature-dependent magnetoconductance plots of Samples A and B.

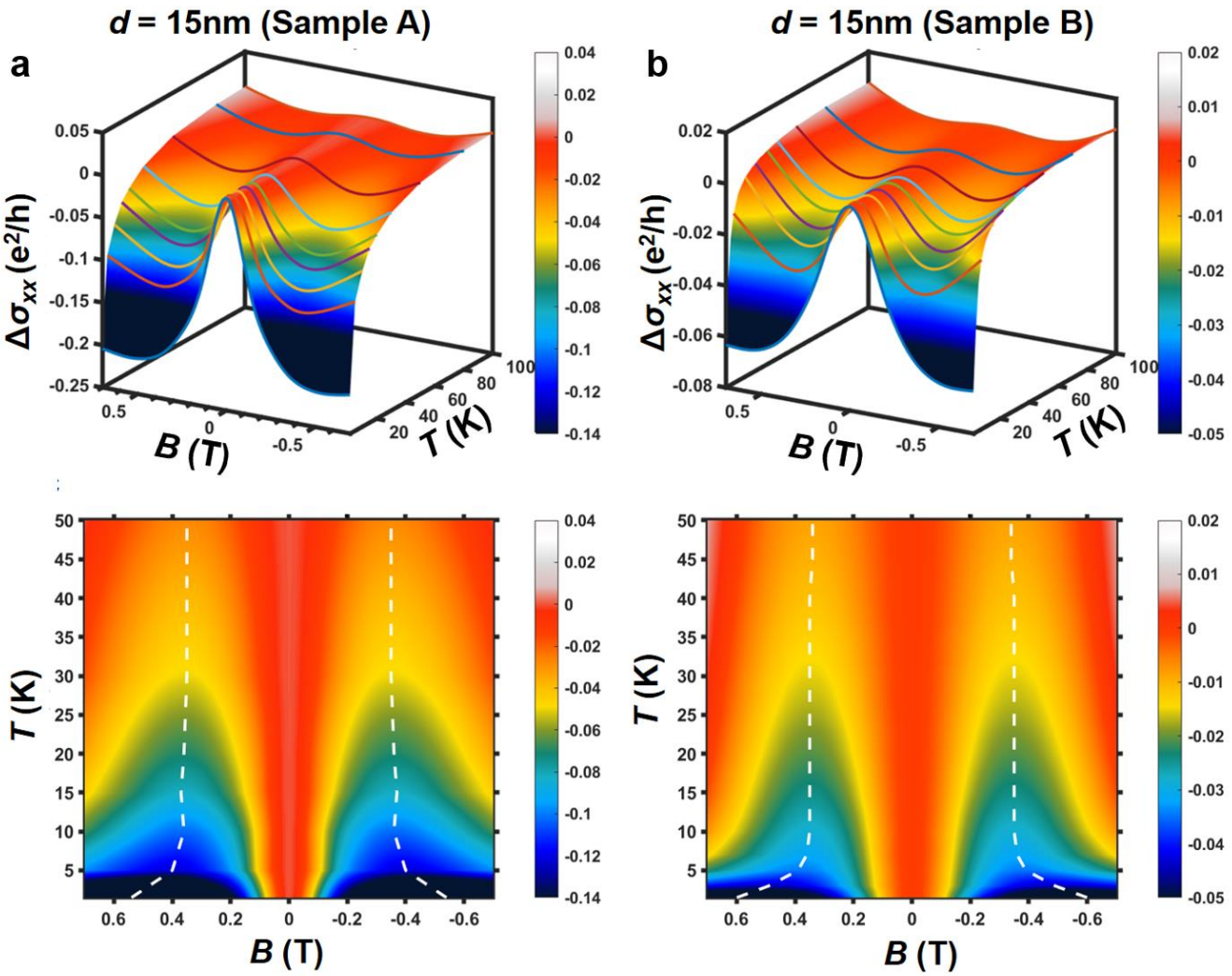

Figure S7. Comparison of the temperature-dependent WAL plots in two InSb(15 nm) /CdTe(1.2 μm) samples with similar carrier density but different carrier mobilities. Figure S7a is re-captured from Figures 2e and 2i.

In Figure 3, we show that with the same InSb layer thickness and carrier density but different carrier mobilities, Sample A and Sample B host almost identical temperature-dependent α_R evolution trend. Here, we further summarize the complete three-dimensional plots of the low-field MC information of the two samples, and the results are presented in Figure S7. Strikingly, both WAL line-shapes resemble each other with respect to temperature and applied magnetic field (the only quantitative discrepancy is the WAL

amplitude). These observations not only justify the universality of the WAL phase diagram of the InSb/CdTe system, but also manifest the indispensable role of the Fermi level position (*i.e.*, carrier density) in determining the interfacial Rashba SOC strength of the heterostructures.

8. Carrier-density distribution of the Al_2O_3/InSb(15 nm)/CdTe device under different gate bias.

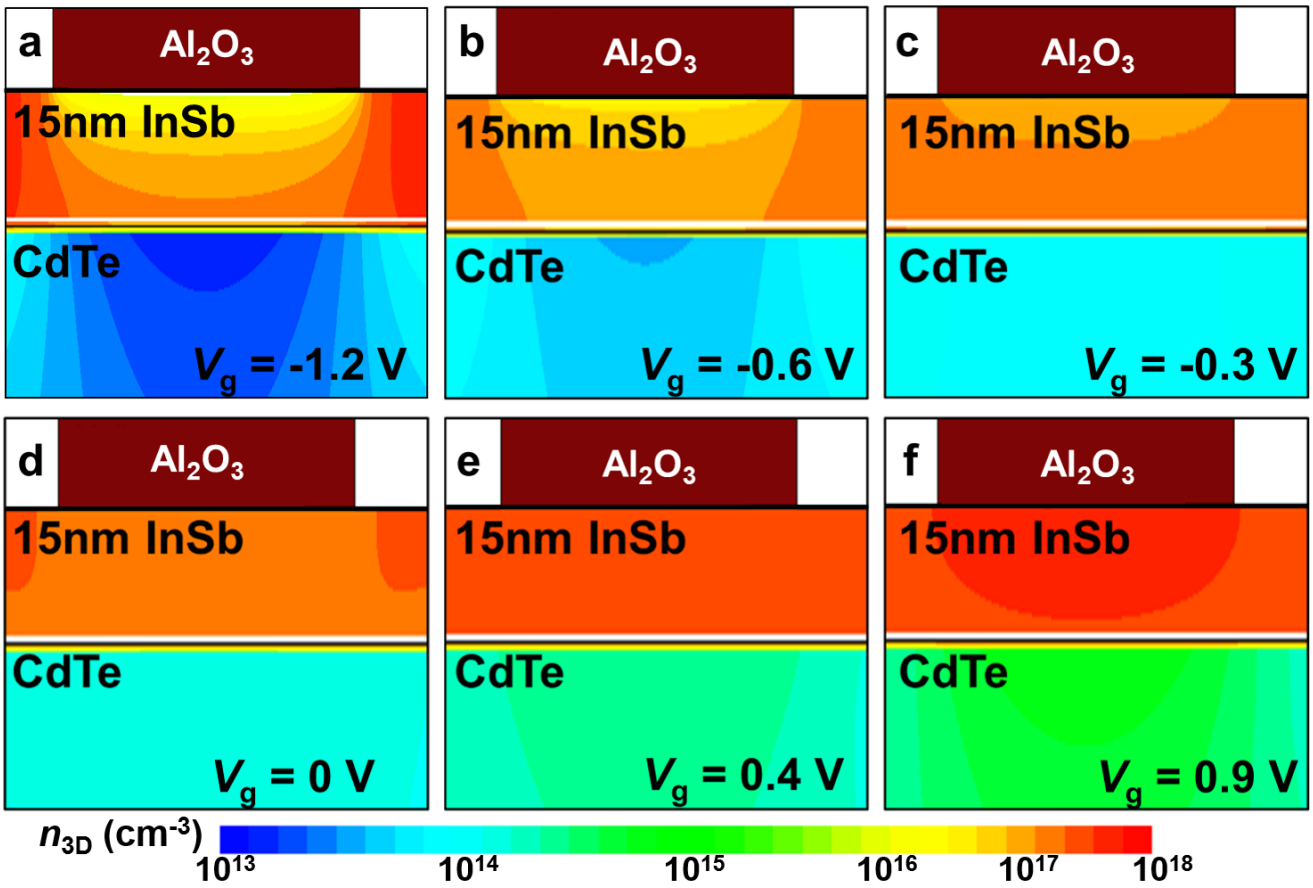

Figure S8. Carrier density distribution profile in the Al_2O_3/InSb(15 nm)/CdTe structure under different top-gate voltage V_g ranging from (a) −1.2 V, (b) −0.6 V, (c) −0.3 V, (d) 0 V, (e) +0.4 V, and (f) +0.9 V, respectively.

Based on the gate-dependent WAL curves shown in Figure 4, it is concluded that the band bending and Fermi level position (*i.e.*, carrier density) may exclusively determine the average Rashba coefficient of the *n*-type InSb(15 nm)/CdTe(1.2 μm) sample. Accordingly, we have used the Sentaurus Device simulator (*i.e.*, commonly-used TCAD software provided by Synopsys) to further quantify the relations among these key parameters. In order to make a solid investigation, the Al_2O_3(50 nm)/InSb(15 nm)/CdTe(1.2 μm) MOS structure is firstly defined by the SDE tools in which the dielectric constant of Al_2O_3 (8.6) and initial InSb layer carrier density (6×10^{17} cm^{-3} at $V_g = 0$ V) are set in reference to the experimental data. During the simulation process, the gate electrode is placed at the top of the Al_2O_3 layer and ground electrodes are

placed at the right/left edge of InSb channel. The designed device structure is later exported to the SDevice tool in which the 2D Poisson solver included both electron and hole is performed to obtain the real-space band diagram and carrier distribution under different gate voltage bias. From the simulated profiles shown in Figure S8, it is obvious that the majority electron conduction channel gradually shifts from the embedded InSb/CdTe interface to the top Al_2O_3/InSb region as the applied V_g varies from −1.2 V to +0.9 V. Consequently, both the enhanced built-in electric field generated at the InSb/CdTe interface and greatly-reduced InSb layer carrier density give rise to the amplified Rashba coefficient in the $V_g < 0$ V regime, whereas the dominated bulk conduction with higher carrier density level yields the negative MC background and weak WAL signature when $V_g > 0$ V.

9. Gate voltage-dependent electron effective mass in the InSb/CdTe heterostructures.

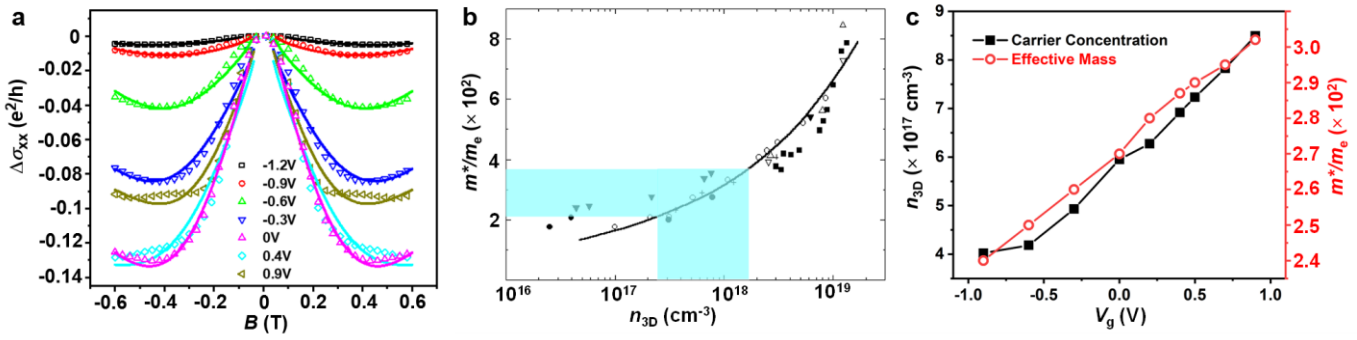

Figure S9. (a) Experimental and ILP-model fitting results of the gate-dependent WAL data of the top-gated InSb(15 nm)/CdTe(1.2 μm) FET device. (b) Electron effective mass as a function of the carrier density of the InSb material. The highlighted blue region corresponds to the carrier densities of the MBE-grown InSb/CdTe samples studied in this work. Re-captured from Ref. 13. (c) Gate-dependence of carrier density and electron effective mass in the InSb/CdTe heterostructures.

In order to understand the gate-dependent Rashba coefficient in our InSb(15 nm)/CdTe(1.2 μm) FET device, we apply the ILP model to fit the MC curves under different applied gate voltage, and the result is summarized in Figure S9a, where the width of the WAL cusp gradually shrinks with the increase of V_g from −1.2 V to 0.9 V. In addition to the WAL width ($\boldsymbol{B_{SO}}$) change, it is known that the electron effective mass m^* is intrinsically associated with the band structure curvature at the Fermi level (*i.e.*, $m^* = \frac{\hbar^2}{(d^2E/dk^2)}$ where E is the energy and k is the momentum).[14] Therefore, the modulation of the Fermi level position and carrier density by the electric field is expected to change the m^* value as well. According to the well-established $m^* - n_{3D}$ relation of the InSb material (Figure R9a),[13, 15] we further plot the gate-dependence of carrier density and electron effective mass in the top-gated InSb(15 nm)/CdTe device, as shown in Figure R9b. It is seen that the reduced carrier density under the negative-biased case also results in a smaller electron effective mass, and the m^* value exhibits an almost linear correlation with the applied gate voltage in the examined region (−0.9 V < V_g < 0.9 V). Such observation therefore not only provides a direct evidence

of the highly-efficient electric-field controlled property of the InSb/CdTe heterostructures, but may also explain the similar linear relation between the Rashba coefficient and the gate voltage given that $\alpha_R = \sqrt{e^3\hbar \boldsymbol{B}_{\mathbf{SO}}}/m^*$.

REFERENCES:

(1) Hall, E. H., On a New Action of the Magnet on Electric Currents. *American Journal of Mathematics* **1879,** *2*, 287-292.

(2) Breunig, O.; Wang, Z.; Taskin, A.; Lux, J.; Rosch, A.; Ando, Y., Gigantic Negative Magnetoresistance in the Bulk of a Disordered Topological Insulator. *Nat. Commun.* **2017,** *8*, 15545.

(3) Caviglia, A.; Gabay, M.; Gariglio, S.; Reyren, N.; Cancellieri, C.; Triscone, J.-M., Tunable Rashba Spin-Orbit Interaction at Oxide Interfaces. *Phys. Rev. Lett.* **2010,** *104*, 126803.

(4) Renard, V. T.; Kvon, Z. D.; Gusev, G.; Portal, J., Large Positive Magneto-Resistance in High Mobility 2D Electron Gas: Interplay of Short and Long Range Disorder. *Phys. Rev. B* **2004,** *70*, 033303.

(5) Dyakonov, M. I.; Perel, V. I., Current-Induced Spin Orientation of Electrons in Semiconductors. *Phys. Lett. A* **1971,** *35*, 459-460.

(6) Hikami, S.; Larkin, A. I.; Nagaoka, Y., Spin-Orbit Interaction and Magnetoresistance in the Two Dimensional Random System. *Prog. Theor. Phys.* **1980,** *63*, 707-710.

(7) Lang, M.; He, L.; Kou, X.; Upadhyaya, P.; Fan, Y.; Chu, H.; Jiang, Y.; Bardarson, J. H.; Jiang, W.; Choi, E. S.; Wang, Y.; Yeh, N. C.; Moore, J.; Wang, K. L., Competing Weak Localization and Weak Antilocalization in Ultrathin Topological Insulators. *Nano Lett.* **2013,** *13*, 48-53.

(8) Niu, C.; Qiu, G.; Wang, Y.; Zhang, Z.; Si, M.; Wu, W.; Peide, D. Y., Gate-Tunable Strong Spin-Orbit Interaction in Two-Dimensional Tellurium Probed by Weak Antilocalization. *Phys. Rev. B* **2020,** *101*, 205414.

(9) Schmidt, H.; Yudhistira, I.; Chu, L.; Neto, A. C.; Özyilmaz, B.; Adam, S.; Eda, G., Quantum Transport and Observation of Dyakonov-Perel Spin-Orbit Scattering in Monolayer MoS_2. *Phys. Rev. Lett.* **2016,** *116*, 046803.

(10) Manchon, A.; Koo, H. C.; Nitta, J.; Frolov, S.; Duine, R., New Perspectives for Rashba Spin–Orbit Coupling. *Nat. Mater.* **2015,** *14*, 871-882.

(11) Nakamura, H.; Koga, T.; Kimura, T., Experimental Evidence of Cubic Rashba Effect in an Inversion-Symmetric Oxide. *Phys. Rev. Lett.* **2012,** *108*, 206601.

(12) Lu, H.-Z.; Shen, S.-Q., Finite-Temperature Conductivity and Magnetoconductivity of Topological Insulators. *Phys. Rev. Lett.* **2014,** *112*, 146601.

(13) Zawadzki, W., Electron-Transport Phenomena in Small-Gap Semiconductors. *Adv. Phys.* **1974,** *23*, 435-522.

(14) Sze, S. M.; Ng, K. K., Metal-Insulator-Semiconductor Capacitors. Physics of Semiconductor Devices, third edition. John Wiley & Sons: Hoboken, New Jersey, USA, **2006**, pp 197-240.

(15) Sniadower, L.; Rauluszkiewicz, J.; Galazka, R. R., Determination of the Effective Mass in n-Type InSb by Means of Magneto-Plasma Reflection. *Phys. Status Solidi* **1964,** *6*, 549-554.